AN EXPERIMENTAL AND COMPUTATIONAL COMPARISON OF THE LOW SPEED AERODYNAMICS OF SQUARE AND CIRCULAR SECTIONED BODIES

Simon A. Prince, Jay Bhatti
City University London

Keywords: *Slender Bodies, Aerodynamics, Vortical flow.*

Abstract

Preliminary results are presented from an ongoing experimental and computational (CFD) study comparing the aerodynamics of a series of circular and square cross-section bodies at low speed. The study aims to analyse the effect of fixing primary boundary layer separation at the sharp corner of the square sectioned body, and the effect of nose shape on the leeside vortical flow regime. Preliminary results tend to confirm that the onset of vortex asymmetry is not linked with asymmetric primary separation lines, but is associated with microscopic surface asymmetry or roughness near the nose apex.

1 Introduction

Recent interest has been focussed on non-circular cross-section bodies for application in missile, booster and aircraft forebody design, where benefits have been identified as more efficient internal storage and improved aerodynamic characteristics. In particular, much work has been published [Refs 1-3] on the aerodynamic characteristics of square cross-section bodies in high subsonic and supersonic flows, but there is a lack of data for low speed, especially involving the analysis of different nose shapes and fineness ratio's as well as base configurations.

An experimental and computational study is therefore currently being undertaken to investigate the low speed aerodynamic behaviour of a family of square cross-section bodies and the associated circular bodies for comparison.

As a sharp nosed-slender cylindrical body encounters flow at increasing angle of attack, the leeward flow pattern goes through several distinct regimes. At angle of attacks above about 5^o the boundary layer separates from the body. The reason for this is the inability of the boundary layer to remain attached in the region of strong adverse pressure gradient. The separated boundary layer sheet possesses a rotational characteristic, or vorticity, due to the higher velocities outward than near the surface. These separated shear layers curl up to form well defined vortices in the leeward quadrants. The onset of separation and subsequent development of these vortices cause a significant increase in the aerodynamic loads, due to vortex suction, and extreme loading non-linearities.

At an angle of attack above a few degrees the boundary layer on the leeward side of a body rolls up to form symmetric vortices. When the angle of attack is increased above around 20^o, the symmetrical pattern gives way to an asymmetric flow field, which may be characterised by the appearance of more vortices. An asymmetric leeside vortex pattern results in an asymmetric imbalance in the suction on the surface of the body, such that considerable side forces can be generated that do not exist with a symmetric vortex pattern.

Both of the symmetric and asymmetric vortex regimes are nominally steady, though the dominant (closest to the surface) vortex can switch from one side of the body to the other. As the angle of attack becomes large the vortex pattern becomes unsteady, the shed vortices move off periodically away from the body surface. The different vortex regimes are summarized in figure 1.

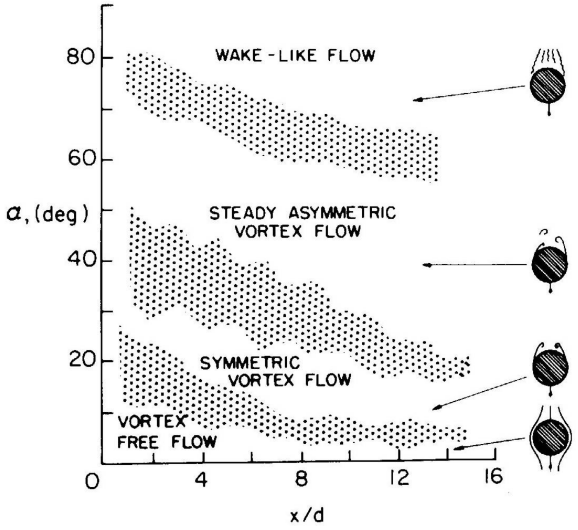

Fig 1: Typical flow regime in the leeside of a slender body at angle of attack [Ref 4]

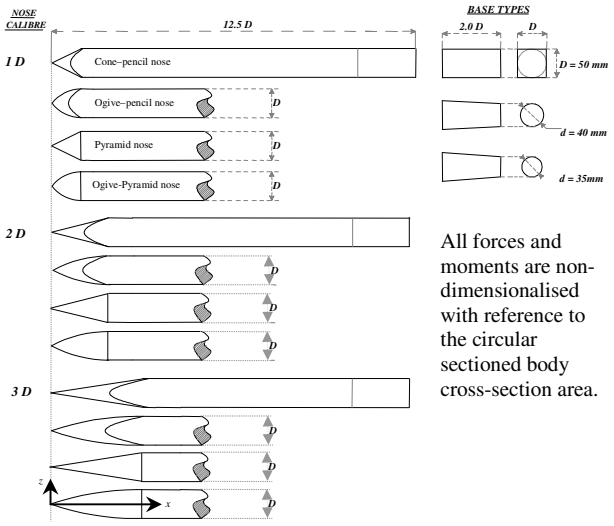

Fig 2: Square and circular section body geometries

While this paper presents initial results for only the three bodies, pictured in figure 3, a series of different bodies has been designed and will be analysed both experimentally (in the City University T2 low speed wind tunnel) and using a modern high resolution commercial Navier-Stokes CFD solver. The bodies under investigation, shown in figure 2, are all 12.5 calibres (diameters) in total length, but differ in the shape and length of the nose section and the boat tail. Four basic nose geometries are being tested. A circular cross-section body can have either a conical nose or an ogival nose. Similarly, a square cross-section body will have either a pyramidal nose or an ogival-pyramid nose, both of which maintain the sharp edge all the way to the nose apex. However, there is often a requirement to have a rounded nose apex for a missile or aircraft nose design. In such circumstances there must be a transition between the square cross-section of the body to a circular cross-section. In this study two transitional nose shapes are being investigated. The cone-pencil nose shape has a linear nose profile, while the ogive-pencil nose has an ogival nose profile. Noses of three lengths, 1, 2 and 3 calibres, will be investigated, as will the effect of a number of different boat-tail configurations.

The study will, in particular, investigate the effect that the different nose geometries on the circular and square cross-section bodies has on the transition between a symmetric and asymmetric leeside vortex regime.

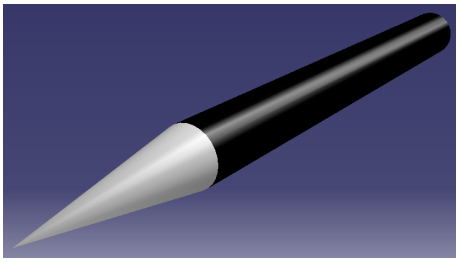

a) 3D conical nose, circular section body

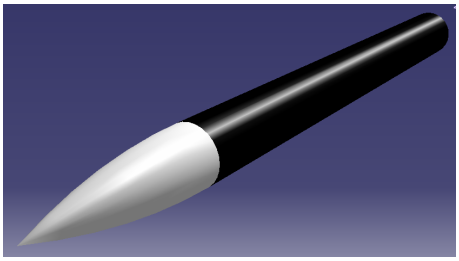

b) 3D ogival nose, circular section body

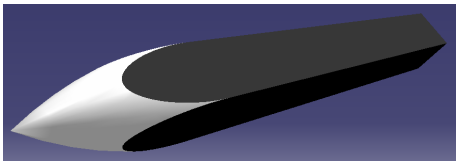

c) 3D ogival-pencil nosed, square section body

Fig 3: Schematic rendering of the bodies tested in study to date.

Past studies have [Refs 5-8] shown that with circular cross-section bodies with smooth

surface boundary layer separation, the onset of vortex asymmetry is not linked with asymmetry in the separation line on either side of the body, but is associated with the sensitivity of the convective flow field to microscopic surface irregularities on the nose tip.

Sharp edges on an aerodynamic surface will fix boundary layer separation. A study performed by Keener and Chapman [Ref 7] tested an aerodynamically sharp leading edge delta wing and showed that even with fixed primary separation, leeside vortex asymmetry still arose. The onset of vortex asymmetry on the leeside of a square cross-section, pyramidal nosed, body should therefore conclusively prove this theory for the origin of the breakdown of the symmetric leeside vortex regime.

2 Experimental and Computational Methodology

2.1 The Wind Tunnel Experiments

Wind tunnel experiments were performed in the City University T2 closed return low speed wind tunnel at Mach numbers between 0.045 (Re_D=51,000) and 0.12 (Re_D=136,000) and for angles of attack between 0 and 40^o and across the full range of roll angles. The T2 wind tunnel working section has measured turbulence levels of 0.5% (turbulent). The models were mounted in the working section on a strut mounted sting system, shown in figure 4, which was connected to the tunnel's computer controlled six component force / moment balance.

Models were first tested with a purely smooth surface (natural transition) and again with a 4mm wide strip of sand-paper roughness located at x/D=0.05 (as shown in figure 4) to fix turbulent boundary layer flow over the body surface.

While some models were made without any surface pressure orifices, such as the one shown in figure 4, others were manufactured with circumferential arrays of 28 pressure orifices, each 13.3^o apart, to measure the circumferential pressure distributions at x/D=2.5, 5 and 7. Surface pressures were measured using a Pressure Systems, Inc. ESP-miniature pressure scanner (rated at ±2.5 psig) and a Chell CANdaq self-contained data acquisition system. Each orifice on the surface was connected, via plastic tubing, to a port on the scanner. Readings from the scanner were sampled by the CANdaq system over a period of 10 s and then relayed to a PC for analysis. Each model was tested three times for repeatability, by undertaking a continuous pitch sweep with constant wind speed, taking data during the pitch-up and pitch-down.

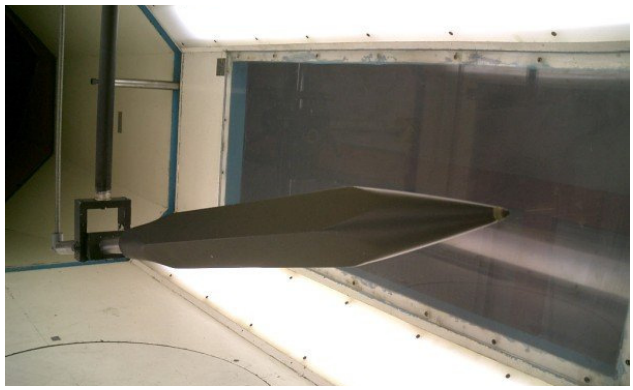

Fig 4: A 3D nosed square cross-section body mounted on the sting system in the T2 wind tunnel working section.

2.2 The CFD Study

A modern 3D steady / unsteady Navier-Stokes solver was also employed, using structured grids with up to ~1 million hexahedral cells, to compute a selection of the cases in order to provide more detailed information on the complicated vortical flows that were seen to develop on the leeside on the bodies. Computational grids were all designed with wall normal cell clustering such that the first cell height was set at $1x10^{-5}D$. The calculations were performed using the Spalart-Allmaras turbulence model such that the computational results can be used to assess the turbulent fixed experimental results.

Both the experimental and the CFD elements of the study are still ongoing, and this paper presents only the initial results for the 3D conical nosed circular cross-section body.

3 Results

The variation of a selection of the measured forces and moments for the 3D conical nosed circular cross-section body is presented in figure

5 for the cases of 0, 90 and 180° roll angle from a prescribed zero roll orientation. These measurements were taken simultaneously with the associated surface pressure measurements, presented at different angles of attack for the station x/D=5, in figure 6. In these plots, ϕ=0° corresponds with the windward attachment line, with the circumferential angle proceeding clockwise viewed from the nose down the body. Figure 7 compares the variation, with angle of attack, of a selection of the measured forces and moments for the 3D ogival nose circular sectioned body, and the corresponding ogival-pencil nosed square cross-section body, while figure 8 presents examples of the CFD resolved leeside flow structure for the turbulent conical nosed circular cylinder case at the axial station *x/D*=5 for α=10° and 20°.

It must be noted that no data is presented for rolling moment or yawing moment. Yawing moment behaves almost exactly as side force, while it was found that the sensitivity of the balance was insufficient to resolve rolling moment accurately.

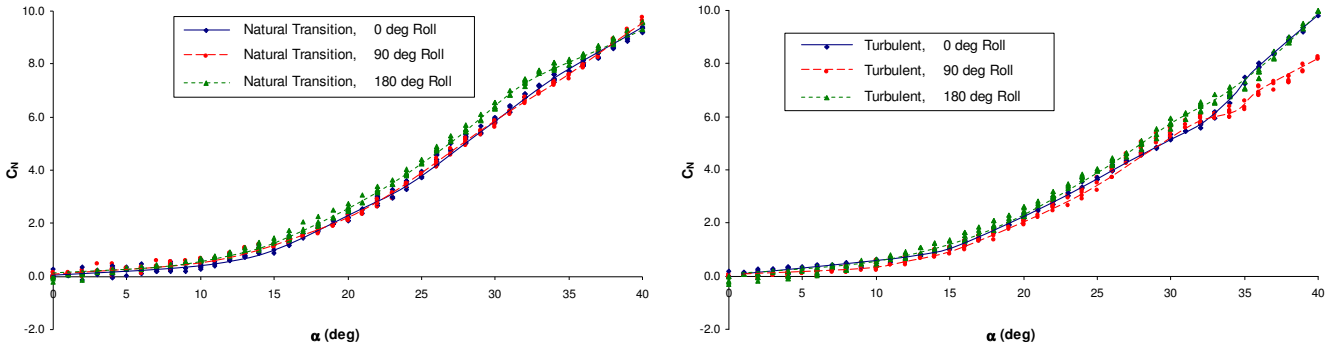

a) Normal force coefficient

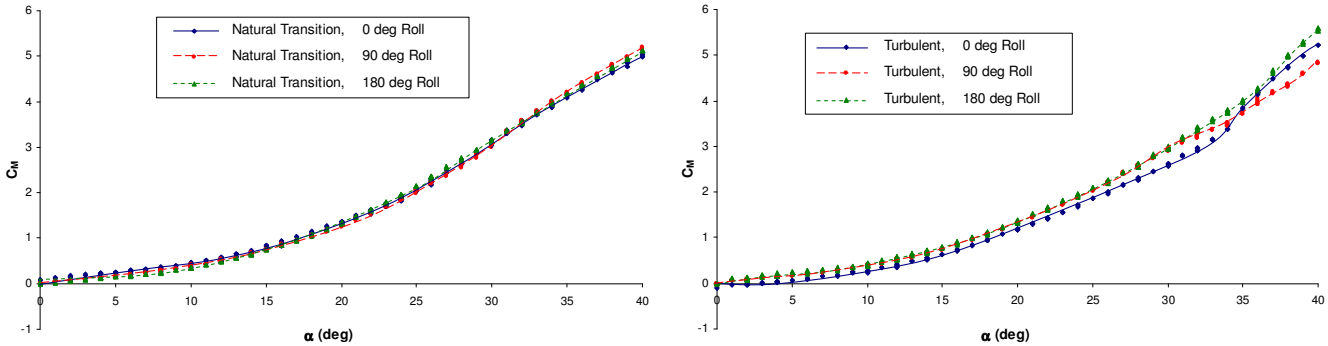

b) Pitching moment coefficient (about sting hinge point at x=0.75m)

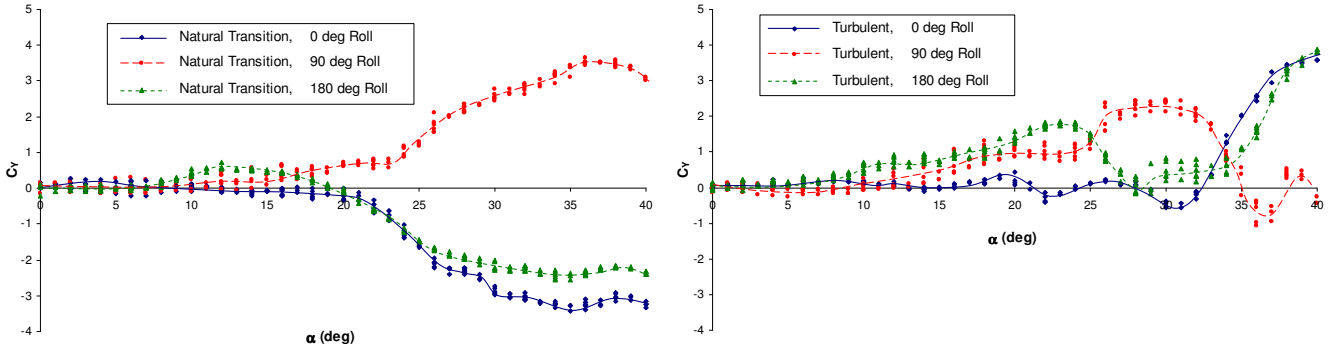

c) Side force coefficient

Fig 5: Comparison of measured and computed aerodynamic characteristics for 3D conical nosed circular cross section body with no boat tail. Re_D=1x10^5.

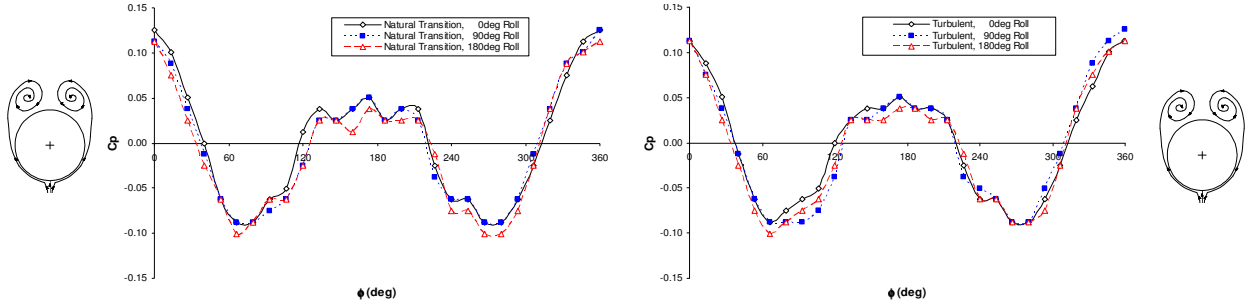

a) $\alpha = 15^o$. Symmetric leeside vortex patterns.

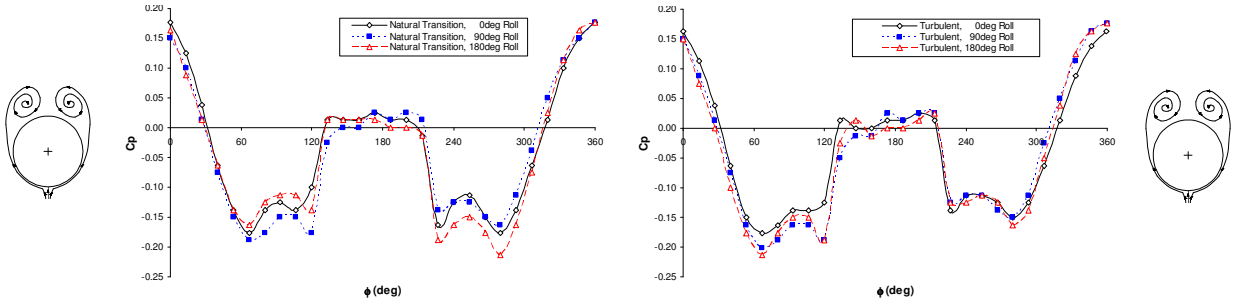

b) $\alpha = 20^o$. Symmetric leeside vortex patterns.

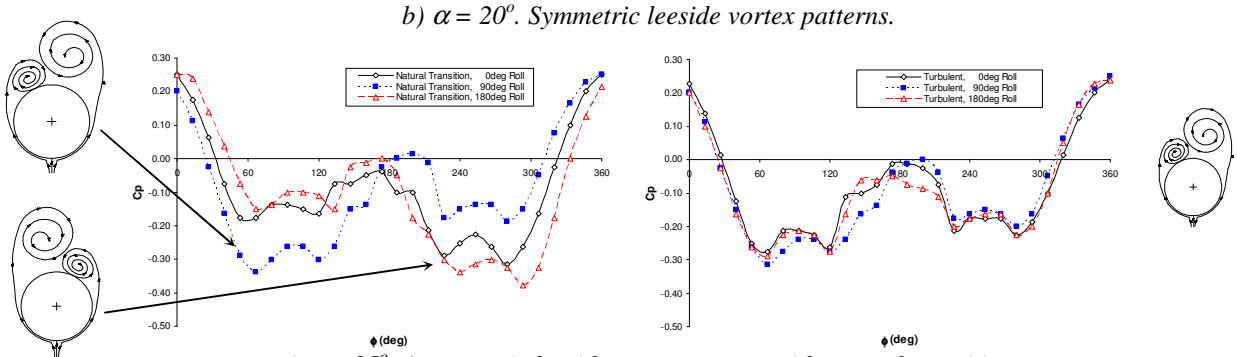

c) $\alpha = 25^o$. Asymmetric leeside vortex pattern with natural transition.

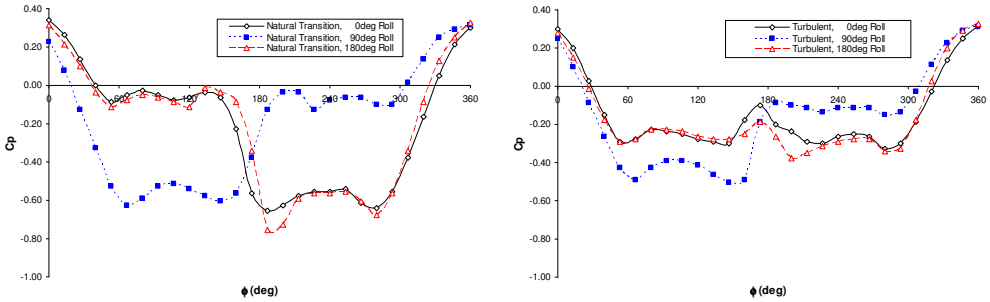

d) $\alpha = 30^o$. Asymmetric leeside vortex patterns for both cases.

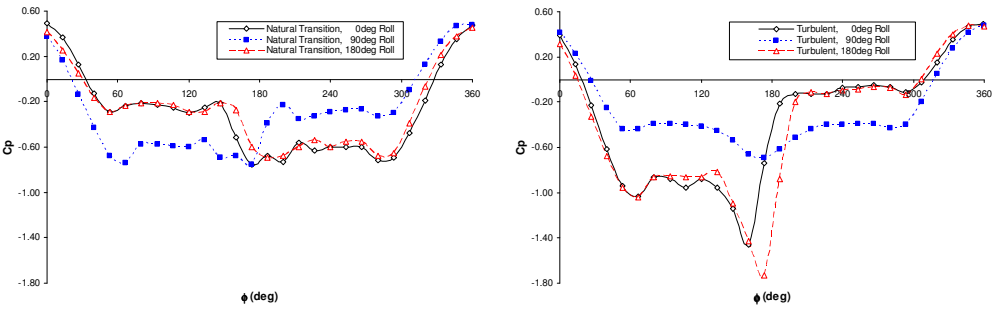

e) $\alpha = 40^o$. Asymmetric leeside vortex patterns for both cases.

Fig 6: Comparisons of surface pressure distributions at an axial plane at x/D=5.0 for three roll orientations. $Re_D=1x10^5$.

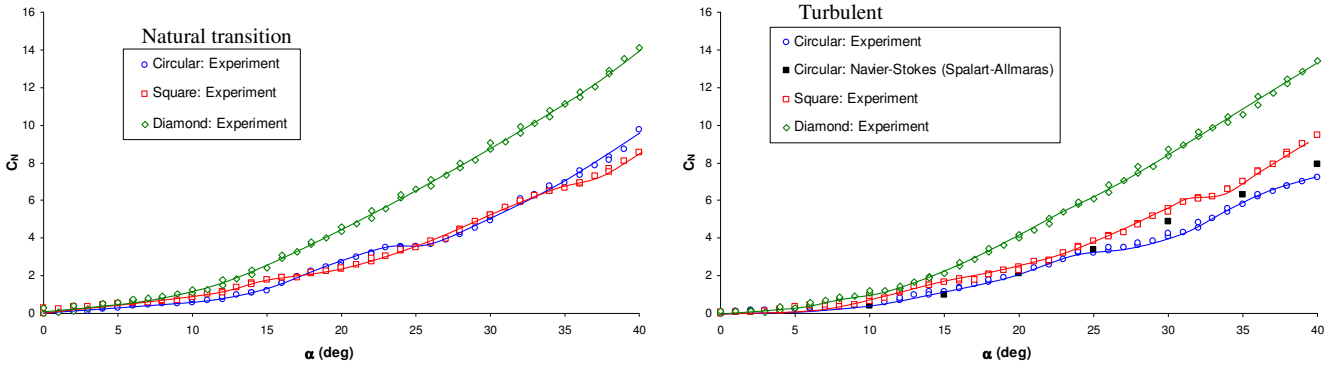

a) Normal force coefficient

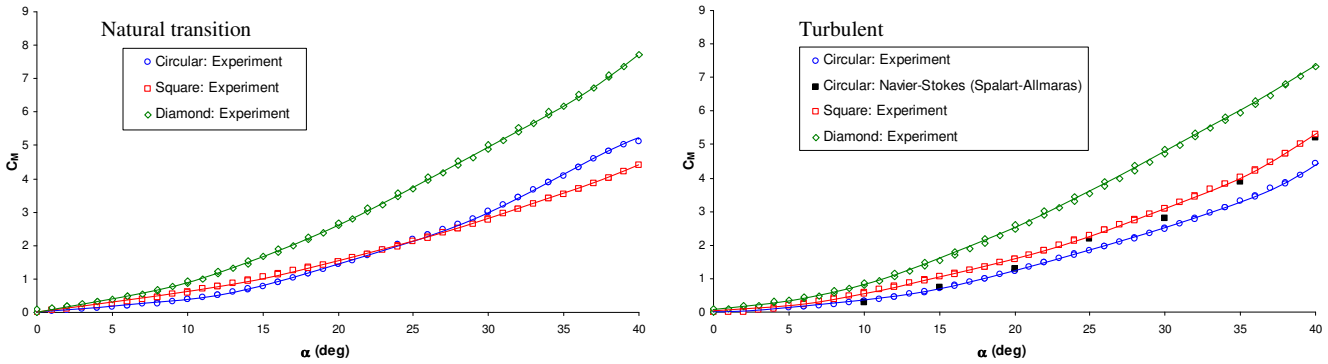

b) Pitching moment coefficient (about sting hinge at x=0.75m)

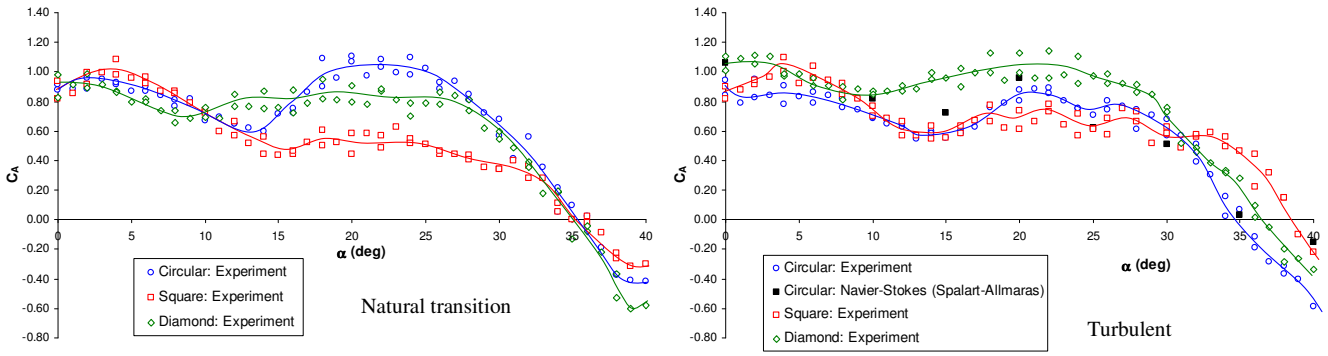

c) Axial force coefficient

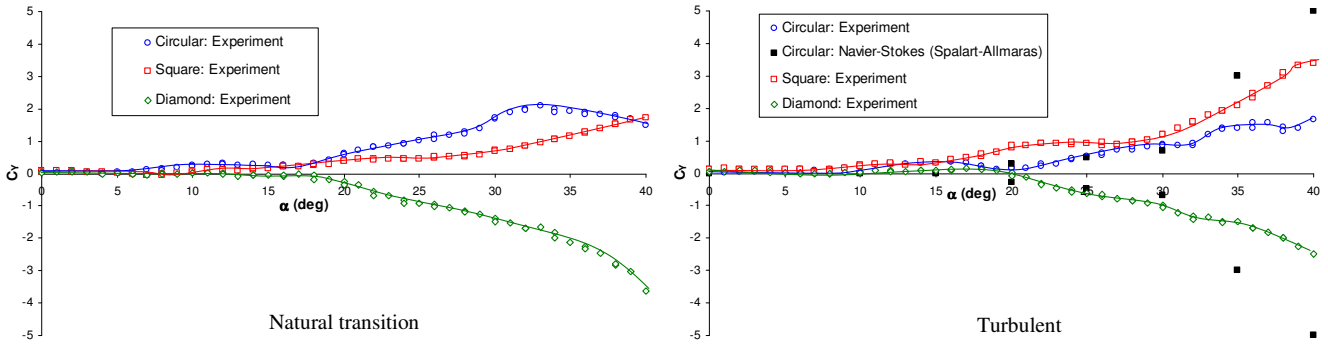

d) Side force coefficient

Fig 7: Comparison of measured aerodynamic characteristics for the 3D ogival nose circular section and 3D ogival-pencil nosed square section body in square and diamond roll orientation. Re_D=1x10^5.

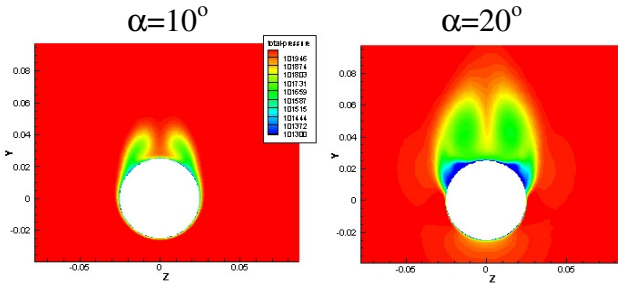

Fig 8: Turbulent Navier-Stokes solution for total pressure at axial slice x/D=5.0. U=35m/s, Re_D=114000.

4 Discussion

The following discussion covers only the data presented in this paper, which represents the initial results in an ongoing study which will cover all of the geometries outlined in figure 2, to gain a more in depth understanding of the low speed aerodynamic characteristics of slender square cross bodies and different nose fineness ratios and profiles.

The results for the 3D conical nosed, circular cross-section body are presented in figures 5 and 6. The circular cross-section body results are being obtained as a baseline for the assessment of the aerodynamic characteristics of the corresponding square cross-section bodies. However, this set of results are interesting in their own right, particularly in that they confirm the findings of other studies regarding the onset of vortex asymmetry and the resulting side force trends.

From figure 6 it can be seen that for both the natural transition case and the forced transition case the surface pressure distributions at x/D=5 exhibit turbulent primary separation behaviour up to α=25°. At α=15° the Cp distribution for both cases appeared to show classic symmetric leeside vortex suction with evidence of secondary vortex suction. Interrogating the measured side force, C_Y, at this angle of attack, however, shows that at ϕ=0° roll there is negligible side force, while at 90° and 180° roll C_Y values of up to ~0.3 are encountered. This is of the same order of magnitude, though slightly lower, as the normal force for these cases. This would seem to suggest that there may be strong vortex suction asymmetries at other axial stations further down the body that account for these side forces. This is evidence that vortex asymmetry in this case appears first towards the rear of the body. The simultaneous measurements of the surface pressure distributions at stations x/D=2.5, 5.0 and 7.0, currently in progress, should shed more light on this issue.

At α=20° slight asymmetries begin to appear in the pressure distributions, with small differences with body roll angle. This corresponds with the higher side forces of ~0.5 – 0.8 for roll angles of 90° and 180° for both cases. For ϕ=0° roll the side force still appears to be negligible, however. This strong sensitivity to roll angle is a classic phenomena associated with asymmetric vortex formation [Refs. 4-8], and has been suggested to indicate strongly that the origin of the asymmetry is in microscopic surface imperfections.

At α=25° with natural transition the sensitivity of the surface pressure distribution to roll angle becomes very marked, while the differences for forced transition at the nose tip (turbulent) remain much less. This is not seen, however, in the side force measurement, where strong roll sensitivity is evident for both cases. For the natural transition case, the dominant vortex (maximum suction) appears on the port (left hand, ϕ=0-180°) side of the body for 0 and 180° body roll angle, but on the starboard side (ϕ=180-360°) for 90° body roll angle. This corresponds with negative side force for 0 and 180° body roll angle and positive side force for 90° body roll angle, where the magnitude is ~1.5 – 2.0 for both cases. For the turbulent, forced transition, case the surface pressure distribution shows that the port side vortex appears to be slightly dominant at this x/D=5.0 station, and remains relatively insensitive to body roll angle. Looking at the side force measurements, however, there is negligible side force for zero body roll angle while at both 90° and 180° roll angle the side force is measured at ~+1.5 for both cases. Again, this discrepancy between surface pressure measurements at x/D=5.0 and the overall side force reading can only be explained if strong vortex asymmetry develops over the rear of the body first, before these effects progress upstream with higher angles of attack.

Between α=25-30^o, careful analysis of the normal force and pitching moment data revealed that slight roll sensitivity appears in the forced transition case, where this is not evident in the natural transition case. In particular the pitching moment for the 0^o degree body roll angle with forced transition is significantly lower than the corresponding cases with 90^o and 180^o roll angle. This suggests that the earlier onset of strong vortex asymmetry and resulting side forces from a dominant primary vortex results in marginally increased overall normal force. Such roll sensitivity in this angle of attack range is not seen for the natural transition case, where relatively large side forces are experienced in all three roll orientations.

At α=30^o significant surface pressure asymmetry is evident in both the natural and forced transition (turbulent) cases. With natural transition the dominant vortex appears on the starboard side for 0^o and 180^o roll angles (corresponding with negative side force coefficient) but on the port side for 90^o roll angle (corresponding with positive side force coefficient). Interestingly the magnitude of the side force, whether positive or negative, is practically the same. This agrees with previous results from other studies [Refs. 4-8]. For the forced transition case the asymmetry in the pressure distribution at x/D=5.0 for roll angles of 0 and 180^o appears minimal compared with that seen at 90^o roll angle. This corresponds with low measured side forces (~ ±1.0) for 0^o and 180^o roll but much higher values (C_Y ~ +2.5) at 90^o roll angle.

Between α=30^o-40^o, the forced transition cases continue to show sensitivity to body roll angle, as the normal force and pitching moment measurements for 0^o and 180^o roll angle cases show a marked increase with angle of attack, in contrast to the previous trend. Strong asymmetry indicated in the pressure distribution at x/D=5.0, for the forced transition case for 0^o and 180^o roll angles, correspond with higher normal force and pitching moment trends compared with ϕ=90^o where the pressure distribution appears to be more symmetrical, corresponding with low measured side force. The natural transition cases continue to show insensitivity to roll orientation for normal force and pitching moment, for which the side forces for all roll cases continue to remain high (C_Y~ ±4.0). At α=40^o, the pressure distributions for the forced transition cases show peak suction occurring at the portside for both the 0^o and 180^o roll angle cases, thus confirming the corresponding positive side forces observed (C_Y ~ +4.0). The pressure distributions for the natural transition, 0^o and 180^o roll cases show peak suction occurring on the starboard side of the body, corresponding to the large negative side forces observed. The corresponding 90^o roll case shows peak suction present on the port side, thus verifying the large positive side force observed for this case. The magnitude, positive or negative, of these forces is seen to be practically equivalent.

Figure 9 presents the relationship between the maximum recorded side force with crossflow Mach number. The solid line presents the boundary representing the accumulated data from many past studies, presented by Wardlaw [Ref 4], while the dot indicates the maximum side forces experienced in the present study. Clearly the present results conform well with past experiment.

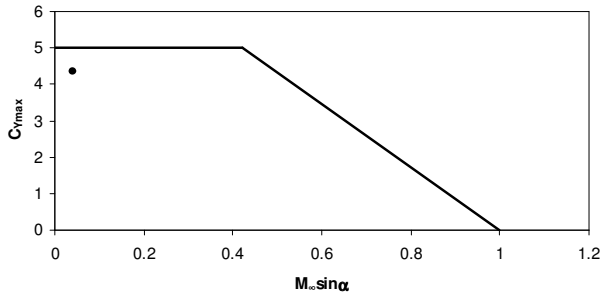

Fig 9: C_{Ymax} variation with crossflow Mach number [Ref 4] with present data as dot.

The aerodynamic characteristics of a circular cross-section body with a 3D tangent-ogive nose is compared with the corresponding data for a square cross-section body with a 3D ogival-pencil nose in figure 7. The data include the CFD predictions obtained from the Navier-Stokes code with the Spalart-Allmaras turbulence model to simulate the forced transition case. What is immediately obvious is that the square cross-section body in diamond roll orientation generated considerably more normal force and pitching moment (based on the

model hinge location at x=0.75m) than either the same model in the square roll orientation or the circular cross-section body. This is to be expected since in the diamond orientation the body presents considerably more (by a factor of almost $\sqrt{2}$) planform area to the crossflow than the other two cases. Interestingly, however, if the non-dimensionalisation was performed with reference to the planform area rather than the cross-section area of the circle (see figure 2) the diamond orientation would be seen to still give values of C_N and C_M higher than the other configurations since the sharp edges force the earlier development of the primary vortices, which at a given station will therefore be stronger. The vortex lift from the diamond orientation will therefore be higher than for the square orientation or the circular cross-section body.

Interestingly even though the square cross-section body in the square orientation has sharp edges that will fix primary boundary layer separation, the normal force and pitching moment curves do not differ greatly from those obtained for the circular cross-section body with natural transition up until α=30°. While the CFD analysis, that has yet to be completed for the square body will reveal the detailed flow structure, it is expected that the lower (windward) sharp edges force the formation of elongated "ear" like vortical structures on the sides of the body which do not contribute to lift, while the upper sharp edges force the formation of primary vortices that act very similar to those seen with the circular cross-section body. Above α=30° with natural transition, the circular cross-section body actually delivers higher normal force and pitching moment than the equivalent square orientation, square cross-section body.

For the forced transition (turbulent) case the square cross-section body in square orientation is seen to generate marginally higher normal force and pitching moment up to α~25°, and increasing greater levels with higher angle of attack. It is not immediately obvious why this is the case and it is expected that Navier-Stokes CFD solutions will be able to reveal the physics behind this effect. For the circular cross-section body, for which a full CFD pitch sweep has been performed, the agreement between the predicted normal force and pitching moment and the measured data appears to be very good up to α=30°, but CFD is seen to overpredict the normal force and pitching moment at the higher angles of attack. Figure 8 presents the CFD resolved leeside vortex structure in the crossflow plane of the circular cross-section body at axial station x/D=5.0 for α=10 and 20°. This CFD model uses a full 360° structured grid which allows the numerical resolution of vortex asymmetry. The numerical solutions, however, predict that up to α=20° the leeside vortices remain in symmetric pattern (although slight asymmetries are visible at α=20°).

The experimental axial force data, being the most sensitive component to measure, exhibits considerable experimental scatter, but the experimental resolution of the balance (C_A=±0.1 at U=30m/s) is sufficient to resolve the general trends. Surprisingly the turbulent CFD solutions for the forced transition case are seen to have resolved the axial force trend for the forced transition case remarkably well.

Figure 7d presents the results for measured and CFD (for the forced transition case) resolved side force coefficient. It is important to make the distinction between the experimental measurements, which are the averaged readings over the 10 second scanning period, and do not reflect any unsteadiness and the CFD solutions which were run in time accurate, unsteady mode, in order to resolve the dynamics of the fluctuating leeside vortical flowfield. The CFD data is therefore plotted showing only the maximum (positive and negative) side force coefficient.

For the natural transition models the side forces were measured to be practically zero up to α=6° for the circular body and square cross section body in square orientation, but remains zero up to α~17° for the square cross-section body in diamond orientation. Between 6 and 17° angle of attack, the circular and square orientation bodies exhibited small levels of measured side force (C_Y < 0.2) which is well above the accuracy of the tunnel balance of C_Y=±0.02 for U=30m/s. This may be a result of the small amount of vibration on the model and mounting system during the experiments at this

angle of attack range. At α=17-18^o, however, something physical occurs, which results in a steady rise in the average side force level for all three cases. This corresponds with a significant change in the measured axial force trends. Clearly this is associated with the onset of vortex asymmetry. While the circular cross-section body and the square cross-section body in square orientation display positive side force behaviour, in diamond orientation negative side forces are generated.

The same behaviour is observed with the forced transition cases, where the CFD solutions are plotted for comparison. It is important to note at this point that while the experimental model has microscopic surface irregularities and will experience wind tunnel flow with 0.5% turbulence levels, the only source of instability in the CFD model is numerical dissipation. It is therefore a remarkable result that up to α=30^o the measured average side force is in close agreement with the maximum computed side force. From this it can be inferred that up to this angle of attack the vortex asymmetry is steady, with very little fluctuation, and this is borne out by the CFD analysis. Above 30^o angle of attack, however, the maximum CFD predicted side forces are seen to be considerably higher than the average measured side force levels. The CFD solutions revealed that at these highest angles of attack the leeside flow is highly unsteady, which would explain the much lower average measured value. Also, while the CFD numerical dissipation does not give rise to any preferred dominant vortex pattern, the specifics of the surface irregularities of the experimental model surface dictate whether the side force is positive or negative. Another important result from the CFD study was found to be that vortex asymmetry does indeed appear to have greatest effect first from the rear of the body, with the effect moving progressively upstream with higher angle of attack.

5 Conclusions

The results presented in this paper are the first in an ongoing study, so no definitive conclusions can be presented at this stage. However, the general findings have all been consistent with those from previous studies. The experimental and computational data presented in this paper confirms that the source of vortex asymmetry is not associated with asymmetric separation, and supports the view that it originates from microscopic surface irregularities near the nose tip. The data also suggests that vortex asymmetry appears to have greatest effect first from the rear of the body, with the effect moving progressively upstream with higher angle of attack.

Time accurate CFD Navier-Stokes (Spalart-Allmaras) computations for the circular section body were found capable of resolving the transition of the leeside vortex structure from the steady symmetrical to the steady asymmetrical state, and finally to unsteady asymmetrical shedding state.

References

[1] Daniel, D. C., Lijewski, L. E., & Zollars, G. J. “Experimental Aerodynamic Studies of Missiles with Square Cross Sections”, AGARD CP-336, “Missile Aerodynamics”, September 1982.

[2] Schnieder, W. “Experimental Investigation of Bodies with Non-Circular Cross Section in Compressible Flow” AGARD CP-336, “Missile Aerodynamics”, September 1982

[3] Brebner, G. G., Osborne, W. K., Brown, D. E. “Force and Moment Wind Tunnel Measurements at Mach Numbers From 0.6 to 2.0 on a Body of Square Cross-Section, Alone and in Combination with Cruciform Delta Wings of Aspect Ratio 0.52”. RAE TR 81035, March 1981.

[4] Wardlaw, A. B. “High Angle of Attack Missile Aerodynamics” AGARD Lecture series (Missile Aerodynamics), 1979.

[5] Champigny, P. “High Angle of Attack Aerodynamics”, AGARD Special Course on ‘Missiles Aerodynamics’, June 1994.

[6] Lamont, P. J. “The Complex asymmetric flow over a 3.5D ogive nose and cylindrical afterbody at high angles of attack” AIAA Paper 82-0053.

[7] Keener, E. R. Chapman, G. T. “Similarity in vortex asymmetries over slender wings and bodies. AIAA Journal, vol. 15, No 9, Sept 1977.

[8] Dexter, P. C. Hunt, B. L. “The effect of roll angle on the flow over a slender body of revolution at high angles of attack. AIAA Paper 81-0358.

Copyright Statement